Nano Research
2022, 15(7): 5873–5883

ISSN 1998-0124 CN 11-5974/O4
https://doi.org/10.1007/s12274-022-4230-9

Research Article

Microwave-assisted molybdenum-nickel alloy for efficient water electrolysis under large current density through spillover and Fe doping

Ya-Nan Zhou, Hai-Jun Liu, Zhuo-Ning Shi, Jian-Cheng Zhou, Bin Dong (✉), Hui-Ying Zhao, Feng-Ge Wang, Jian-Feng Yu, and Yong-Ming Chai (✉)

State Key Laboratory of Heavy Oil Processing, College of Chemistry and Chemical Engineering, China University of Petroleum (East China), Qingdao 266580, China

Received: 27 November 2021 / **Revised:** 11 February 2022 / **Accepted:** 13 February 2022

ABSTRACT

The development of high-efficiency electrocatalysts for overall water splitting under large current density is significant and challenging. Herein, a high-performing Fe-doped MoNi alloy catalyst (M-H-MoNiFe-50) abundant with flower-like nanorods assemblies has been prepared by high-pressure microwave reaction and hydrogen reduction. Firstly, Fe doped $NiMoO_4$ precursor (M-MoNiFe-50) was synthesized by microwave fast heating, ensuring the robustness of nanorods, which owns larger area and improved catalytic activity than that by conventional hydrothermal method. Secondly, M-MoNiFe-50 was reduced in H_2/Ar to fabricate Fe-incorporated $MoNi_4$ alloys (M-H-MoNiFe-50), greatly enhancing the conductivity and facilitating hydrogen/oxygen spillover. The final M-H-MoNiFe-50 exhibits remarkable activity for alkaline/acidic hydrogen evolution reaction and oxygen evolution reaction with low overpotential of 208 (alkaline), 254 (acid) and 347 mV at 1,000 mA·cm^{-2}. Moreover, an alkaline water electrolyzer is established using M-H-MoNiFe-50 as anode and cathode, generating a current density of 100 mA·cm^{-2} at 1.58 V with encouraging durability of 50 h at 1,000 mA·cm^{-2}. The extraordinary water splitting performance can be chalked up to the large surface area, favorable charge transfer, modified electron distribution, intrinsic robustness as well as an efficient gas spillover of M-H-MoNiFe-50. The final electrocatalyst has great prospects for practical application and confirms the significance of Fe doping, microwave method and spillover effect for catalytic performance improvement.

KEYWORDS

high-pressure microwave, Fe doping, $MoNi_4$, spillover, overall water splitting

1 Introduction

Increasingly serious energy and environmental problems impel researchers more intense attention and painstaking effort into the utilization of renewable energy to finally conduct sustainable development. Electrolysis of water to produce hydrogen is a significant pathway to bridge the gap between energy supply and green development as well as low carbon emission [1–3]. Therefore, advanced electrocatalysts that can simultaneously motivate the two half-cell reactions of water splitting (hydrogen evolution reaction (HER) and oxygen evolution reaction (OER)) at high current density is necessitated.

At present, the earth-abundant materials with praisable electrocatalytic performance remain the research's focus because of low cost and large reserves. However, many reported catalysts can only promote a single half-reaction and perform poorly for another electrode reaction [4–6]. In addition to high catalytic activity, stability at high current density is another equally crucial challenge. Practically, considering the commercial application, catalysts that can boost the overall water spitting (OWS) efficiently and durably simultaneously are much more intriguing. Ni-Mo alloys featured with excellent corrosion resistance and good electron transfer capability are deemed as a promising candidate for HER. However, the OER performance is less favorable, thus leading to low OWS efficiency. Especially under large current, the OWS performance remains a challenge [7, 8]. Therefore, necessary tactics are required to further optimize the surface properties, including adsorption capacity and intrinsic electron transport, to facilitate hydrogen evolution. It has been widely accepted that heteroatom doping is a proven and effective strategy to perturb the usual path of electrons, coordination number and bond distance [9–11]. Specifically, Fe with an atomic radius different from Ni can inject electrons into $MoNi_4$ lattice, leading to diverse electronic behaviors, and thus an enhanced OWS performance can be expected. Moreover, under appropriate conditions, the MoNi alloy system can induce the hydrogen spillover effect, which is a well-known phenomenon in heterogeneous catalysts and has been regarded as potential means to boost HER performance for bi-component or multi-component catalysts with different hydrogen adsorption capacities [12]. Analogously, oxygen spillover can also take place on appropriate materials, including Pt, Zr and Mo-based catalysts and so forth [13–15]. Among them, MoO_x species can promote oxygen spillover by accepting the transferred oxygen intermediates

Address correspondence to Bin Dong, dongbin@upc.edu.cn; Yong-Ming Chai, ymchai@upc.edu.cn

from the active center [15]. Given the fact that the interaction between active species and supports leads to accelerated hydrogen/oxygen species desorption process through the migration of active species from catalytic center to the carriers and finally enhancing catalytic performance, the research of electrocatalytic MoNi system based on spillover can be achieved.

In addition, microwave heating is deemed as an energy-efficient method to fast manufacture materials different from conventional reaction mechanisms [16, 17]. Particularly for heterogeneous mixtures, local heating often occurs at interfaces, resulting in higher temperatures than in bulk phase or unpolarized region [16]. J. M. Serra and colleagues reported a microwave-mediated hydrogen production from water splitting and found that the microwave improved electrical conductivity accompanied by partial reduction of gadolinium-doped CeO_2 [18]. It is worth pointing out that the formed oxygen vacancies can induce self-doping and activation of samples, which may be propitious for the OWS performance elevation.

Herein, a microwave heating and hydrogenation reduction route has been adapted to the fabrication of Fe doped MoNi alloys loaded on nanorod $NiMoO_4$ (M-H-MoNiFe-*t*). Firstly, the well-defined Fe-incorporated $NiMoO_4$ precursor nano-assemblies (M-MoNiFe-*t*) are yielded by fast high-pressure microwave heating, which ensures the structural integrity of materials and the large surface area. Compared with conventional hydrothermal synthesis, increased conductivity and robust structure are observed. Density functional theory (DFT) calculation also reveals the changed electron arrangement induced by Fe incorporation. Secondly, M-H-MoNiFe-*t* is reduced under H_2/Ar atmosphere with morphology well maintained, contributing to the uniform distribution and exposure of active sites and subsequent interfacial hydrogen/oxygen spillover. The final M-H-MoNiFe-50 shows encouraging HER activity in both alkaline and acidic electrolyte under large current density, only requiring 208 and 254 mV to reach 1,000 mA·cm^{-2}. Besides, for the surface reconstructed MoNiFe oxyhydroxides, high OER performance is also realized with an overpotential of 160 and 347 mV at 10 and 1,000 mA·cm^{-2}. For OWS, only 1.58 V is needed at 100 mA·cm^{-2}, superior to benchmark Pt/C(+)//RuO_2(−). More importantly, the durability of 50 h at 1,000 mA·cm^{-2} is obtained for OWS. Overall, this work shows the feasibility of high-pressure microwave, heteroatom doping and spillover effect for advanced electrocatalysts.

2 Experimental

2.1 Synthesis of M-MoNi-*t*, M-MoNiFe-*t*, H-MoNi-*t* and H-MoNiFe-*t*

Firstly, the purchased MoNi foam was cut into small pieces of 1 cm × 2 cm and washed with hydrochloric acid, acetone, deionized water and ethyl alcohol for 20 min, respectively, to remove the oxides and impurities on the surface and then dried under vacuum for later use.

For the synthesis of M-MoNi-*t*, 0.35 g $Ni(NO_3)_2{\cdot}6H_2O$ and 0.37 g $(NH_4)_6Mo_7O_{24}{\cdot}4H_2O$ were added to 30 mL deionized water and stirred for 10 min. Then the resulting homogeneous and transparent solution was poured into a high-pressure microwave reaction kettle containing two pieces of cleaned MoNi foam and heated with microwave at 150 °C for various minutes. After the reaction finished, the final samples were taken out and rinsed with deionized water and ethyl alcohol several times and named M-MoNi-*t*, where *t* means 40, 50 and 60 min.

The synthesis of M-MoNiFe-*t* is similar to M-MoNi-*t* except adding 0.242 g $Fe(NO_3)_3{\cdot}9H_2O$.

The H-MoNiFe-*t* and H-MoNiFe-*t* were obtained with the same procedure by hydrothermal synthesis method using a Teflon-lined stainless steel autoclave. The reaction time was selected to be 50 and 360 min.

2.2 Synthesis of M-H-MoNi-*t*, M-H-MoNiFe-*t*, H-H-MoNi-*t* and H-H-MoNiFe-*t*

The obtained precursors were all heated at 400 °C for 1 h under H_2/Ar (10%/90%) atmosphere with a heating rate of 3 °C·min^{-1}.

2.3 Characterization

Scanning electron microscopy (SEM, JEM 2100F) and transmission electron microscopy (TEM, FEI Tecni G20, 200 kV) were used to characterize the morphology information of all the synthesized samples. The crystal structure of the samples was collected by means of X-ray diffraction (XRD) with Cu Kα radiation (λ = 1.54 Å) on a Brook D8 advance equipment. Energy-dispersive X-ray spectroscopy (EDX) was applied on a Hitachi S-4800 to obtain the elemental composition and distribution of the resulting sample. X-ray photoelectron spectroscopy (XPS) was employed to analyze the surface chemical structure and valence information by a Thermo Fisher K-alpha 250Xi.

2.4 Electrochemical measurements

Electrochemical performance measurements were performed at room temperature by a standard three-electrode system with a Gamry Reference 3000 electrochemical equipment. The cut MoNi foam (MNF) (1 cm × 2 cm) was ultrasonically treated with hydrochloric acid, acetone, ethanol and deionized water, respectively, for 30 min to remove the surface impurity. All electrochemical measurements were conducted under the same conditions in 1.0 M KOH or 0.5 M H_2SO_4. For OER (HER), the obtained samples, Pt foil electrode (graphite rod electrode) and saturated calomel electrode were selected as working electrode, counter electrode and reference electrode, respectively. The scan rate of linear sweep voltammetry (LSV) curves was 5 mV·s^{-1}. All the electrode potentials were converted to reversible hydrogen electrode (RHE) via the Nernst equation: $E_{RHE} = E_{SCE} + 0.0592pH + E^0_{SCE}$ (E^0_{SCE} = 0.245 V). The cyclic voltammetry (CV) curves with different scanning rates were employed to determine the double-layer capacitances (C_{dl}). The stability of the sample was evaluated via both chronoamperometry and fast CV cycles with a rate of 40 mV·s^{-1} for 3,000 sweeps. The frequency of electrochemical impedance spectroscopy (EIS) was gained at a certain potential ranging from 10^5 to 0.1 Hz with an AC voltage of 5 mV. All the (over)potentials in this work were converted to RHE unless otherwise noted.

3 Results and discussion

3.1 Structural characterization of M-H-MoNiFe-*t*

The synthesis of M-H-MoNiFe-*t* was performed in two steps, as illustrated in Fig. 1(a). Using cleaned MoNi foam as support (Fig. S1 in the Electronic Supplementary Material (ESM)), the M-MoNiFe-*t* precursor was prepared by a short high-pressure microwave method at 150 °C. Then the final sample was obtained after calcining in H_2/Ar (v/v, 5/95) atmosphere at 400 °C for 1 h. During this process, the inner Ni would diffuse outward, and the resulting $MoNi_4$ particles decorated on $NiMoO_4$ cuboids [19]. Different microwave time was investigated including 40, 50 and 60 min. The catalyst microwaved for 50 min was screened as the representative to carry out the following characterization and discussion.

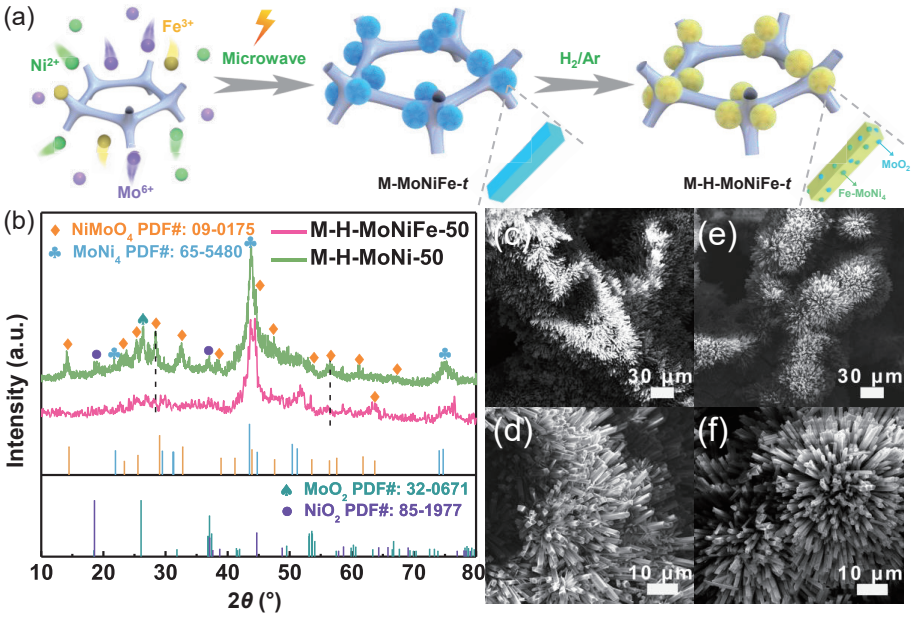

Figure 1 (a) Schematic illustration of the synthesis process of M-H-MoNiFe-t. (b) XRD patterns of M-H-MoNi-50 and M-H-MoNiFe-50. SEM images of ((c) and (d) M-MoNiFe-50 and ((e) and (f)) M-H-MoNiFe-50.

XRD characterization was first detected to analyze the composition and phase of M-MoNiFe-50, M-H-MoNi-50 and M-H-MoNiFe-50 powder stripped from the substrate. Figure S2 in the ESM clearly shows the crystalline structure of $NiMoO_4$ for the M-MoNiFe-50 precursor. In addition, the diffraction peaks at 18.3° and 37.0° can be assigned to the (003) and (101) lattice planes of NiO_2 (PDF#85-1977). The strong peaks around 27.2° come from MoO_2 (PDF#32-0671). After reduction, the newly generated peaks at 21.7°, 43.8° and 75.0° are indexed to the (110), (121) and (312) planes of $MoNi_4$ (PDF#65-5480) (Fig. 1(b)). Interestingly, NiO_2 and MoO_2 species are also observed in partially reduced materials. No Fe species can be discerned due to low content or uniform distribution. Moreover, compared with M-H-MoNi-50, the XRD pattern of M-H-MoNiFe-50 slightly shifts to a lower degree, which is the result of Fe doping.

SEM reveals that the dense flower-like M-MoNiFe-50 nanorod assemblies are perpendicular to the substrate, with the diameter of 0.2–1 μm and lengths of tens of microns (Figs. 1(c) and 1(d)), facilitating the fast release of gas bubbles. The M-H-MoNi-50 and M-H-MoNiFe-50 electrocatalysts show similar morphology grown on the support almost vertically without collapse (Figs. 1(e) and 1(f), and Fig. S3 in the ESM), indicating the good robustness. Note that many nanoparticles are decorated on the M-H-MoNiFe-50 rods, while M-MoNiFe-50 shows a smooth surface (Fig. S4 in the ESM). Using the same process, H-MoNiFe-50 was synthesized via the conventional hydrothermal method for 50 min to compare the potential structural changes. Figure S5 in the ESM manifests that numerous cluttered cuboids align on the substrate and the structure of calcined H-H-MoNiFe-50 has no discernible changes. Further, considering the time-saving properties of microwaves, the hydrothermal time was prolonged to 6 h to prepare H-MoNiFe-360 and H-H-MoNiFe-360. As shown in Fig. S6 in the ESM, for H-MoNiFe-360, flower-like assemblies composed of uneven rods (0.2–7 μm) are obtained with obvious MoNiFe species particles. After further reduction, the rods broke and collapsed, which would decrease the available surface area. This result suggests the rapid and effective heating of the microwave.

The TEM images in Figs. 2(a)–2(c) confirm the presence of nanoparticles of about 10–20 nm on the cuboids. High-resolution TEM of M-H-MoNiFe-50 displays three different lattice spacings (Figs. 2(d)–2(f)), which consist of distances of 0.214, 0.404 and 0.342 nm, corresponding to the (121) and (110) facet of $MoNi_4$ and ($\bar{1}$11) plane of MoO_2, respectively. Figure 2(g) schematically demonstrates the Fe doped $MoNi_4$ crystal. The scanning TEM-EDX characterization in Fig. 2(h) indicates the uniform distribution of Mo, Ni and Fe elements on a single nanorod with the ratio of 16:45:10 (Table S1 in the ESM), which coupled with XRD results confirms the successful incorporation of Fe. The cooperative functioning of the components is expected to be optimally expressed thanks to its favorable space distribution, in which the H-atoms created on Ni rapidly migrate to the neighboring Mo atom [12].

The microchemical environments and surface valence states of M-H-MoNi-50 and M-H-MoNiFe-50 were investigated by the XPS method. As illustrated in Fig. S7 in the ESM, the XPS spectrum proves the presence of Mo, Ni, Fe and O again. For Mo 3d spectra (Fig. 3(a)), three valence states can be analyzed: Mo^0 $3d_{5/2}$ located at 227.8 eV and Mo^{4+} $3d_{5/2}$ at 228.3 eV, Mo^{5+} $3d_{3/2}$ at 231.2 eV, respectively [20]. For M-H-MoNi-50, the contents of Mo^{4+} increase and the peaks shift to higher binding energy, implying that doped Fe perturbs the electronic structure of Mo. For the Ni 2p region (Fig. 3(b)), the fitted peaks at 854.8 and 872.6 eV originate from Ni0 [21]. Besides, Ni^{2+} species are also detected at 855.9 and 874.0 eV [22]. Compared with M-H-MoNi-50, the XPS peaks move to low binding energy, suggesting a decreased valence state after Fe incorporation.

The Fe 2p spectrum (Fig. 3(c)) can be deconvoluted into two peaks at 707.0 and 714.6 eV accompanied by satellite peaks, which are ascribed to Fe^0 and Fe^{2+} species [23]. The O 1*s* spectra (Fig. 3(d)) contain the metal–O (O1 at 530.0 eV), chemisorbed oxygen (O2 at 530.7 eV) which belongs to the hydroxyl-like groups or defect-oxides, and the hydroxyl group of H_2O (O3 at 531.4 eV) on the surface [24, 25]. Moreover, the ratio of O2/O1 is intertwined with the number of surface oxygen vacancies, and the higher value of 1.39 of M-H-MoNiFe-50 than M-H-MoNi-50 (0.75) manifests more abundant oxygen vacancies [24, 25]. Oxygen vacancies on materials have been reported to be beneficial to the decrease of the energy barrier for spillover to realize reversible hydrogen storage or release [26]. XPS results reveal traces of Fe indeed change the electron density of Mo and Ni, which can be further substantiated by DFT calculation. The simplified $MoNi_4$ and Fe-doped $MoNi_4$ (Fe-$MoNi_4$) models are shown in Fig. 3(e). The calculated density

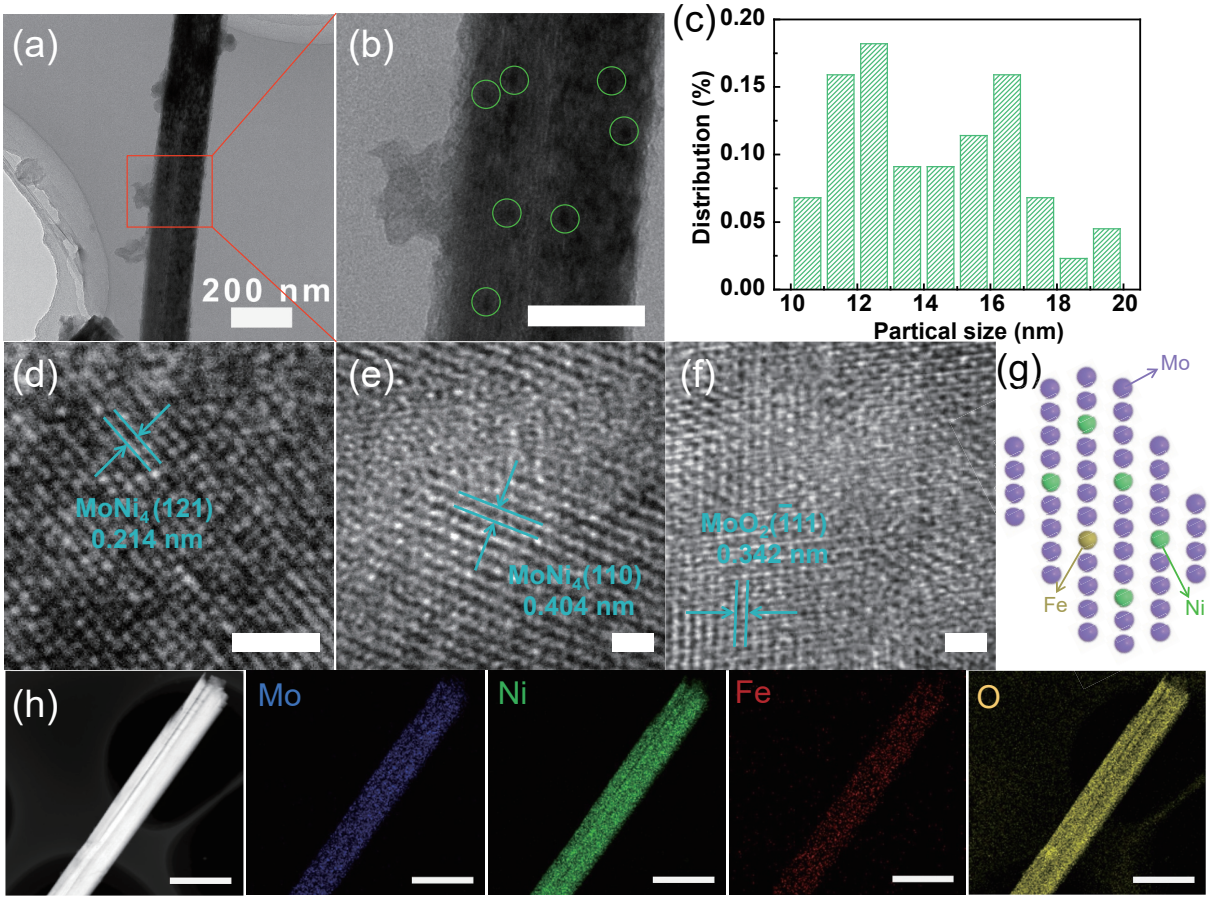

Figure 2 (a) and (b) TEM image of final M-H-MoNiFe-50 sample. (c) Particle size distribution of $MoNi_4$ in M-H-MoNiFe-50. (d)–(f) HRTEM images of M-H-MoNiFe-50. (g) Schematic illustration of Fe doping in $MoNi_4$ crystal. (h) Element mapping of Mo, Ni, Fe and O of single rod in M-H-MoNiFe-50. Scale bar: 1 μm.

of state (DOS) and PDOS (partial DOS) of Fe-$MoNi_4$ are slightly different from those of $MoNi_4$, especially for Ni d-orbital and Mo d-orbital. In addition, the electron density difference simulation of Fe-$MoNi_4$ (Fig. 3(f)) reveals the increased electron density (cyan) of Ni and decreased electron density (yellow) of Mo after Fe introduction, consistent with previous analyses, and thus a modulatory dissociation of water and adsorption of hydrogen can be expected. Moreover, the sparse electron cloud density allows Mo to directly receive the overflowed nucleophilic oxygen [15].

3.2 Electrocatalytic performance for HER, OER and OWS

In order to elucidate the significance of microwave and Fe for M-H-MoNiFe-50, the electrocatalytic HER, OER and OWS performance of all obtained samples were measured with a three-electrode system with iR-correction at room temperature. Firstly, the HER performance was evaluated in 1.0 M KOH. All of the following potentials have been converted to the reversible hydrogen electrode (RHE) unless otherwise noted.

The linear sweep voltammetry (LSV) curves of different microwave time were first collected and plotted, as shown in Fig. S8(a) in the ESM. The optimized M-H-MoNiFe-50 sample with reaction time of 50 min was selected for comparison. Besides, the hydrothermal time was also adjusted to eliminate the influence of morphology. Expectedly, H-H-MoNiFe-50 shows lower activity (Fig. 4(a) and Fig. S8(b) in the ESM), which may result from the modified surface by microwave heating bestows it with specific HER activity [16]. The final LSVs in Fig. 4(a) show the HER activities of M-MoNi-50, M-MoNiFe-50 and H-MoNiFe-300 all increase after reduction in H_2/Ar. Among them, M-H-MoNiFe-50 exhibits the best electrocatalytic activity with a low overpotential of 36 and 208 mV at 10 and 1,000 mA·cm^{-2}, superior to H-H-MoNiFe-300, M-H-MoNi-50 and other reported catalysts (Fig. 4(b) and Table S2 in the ESM), suggesting the improvement of microwave treatment and Fe doping for hydrogen evolution. The calculated Tafel plots show the lowest slopes of 37.6 mV·dec^{-1} for the target M-H-MoNiFe-50, much smaller than those of M-H-MoNi-50 (89.7 mV·dec^{-1}), M-MoNiFe-50 (99.7 mV·dec^{-1}) and H-H-MoNiFe-300 (63.2 mV·dec^{-1}) (Fig. 4(c)), indicating a fast improved current density with the increase of the same overpotential [27, 28]. The low Tafel slope is near to 40 mV, indicating the rate-determining step (RDS) is the Heyrovsky step [20, 30].

Electrochemically active surface area (ECSA) can be employed to explain some catalysts' high activity, which is proportional to the double-layer capacitance (C_{dl}). Figure S9 in the ESM shows the computed C_{dl} via CV curves; the C_{dl} values of M-H-MoNiFe-50 and H-H-MoNiFe-300 both increase after reduction, which may be due to the formed nanoparticles on the nanorods. The smaller C_{dl} of M-H-MoNiFe-50 (6.7 mF·cm^{-2}) than H-H-MoNiFe-300 (8.7 mF·cm^{-2}) means a higher intrinsic activity of M-H-MoNiFe-50. As verification, we then normalized the LSV polarization curves with ECSA, as shown in Fig. S10 in the ESM, suggesting the preferable hydrogen evolution of M-H-MoNiFe-50 and proving that the intrinsic activity was enhanced by microwave pretreatment and subsequent Fe doping. As discussed above, microwaves can potentially lead to activation of materials by highly localized heating while exotic Fe can tailor electron density to modulate water dissociation and hydrogen adsorption [16]. EIS was also measured and fitted via the equivalent circuit given in Fig. 4(d) The resulting M-H-MoNiFe-50 has the smallest semicircle diameter among the different samples, and the diameter gradually reduces in the sequence of H-MoNiFe-300, M-H-MoNi-50, H-H-MoNiFe-300, M-MoNiFe-50 and M-H-MoNiFe-50, indicating the charge transfer capability has been synergistically strengthened by

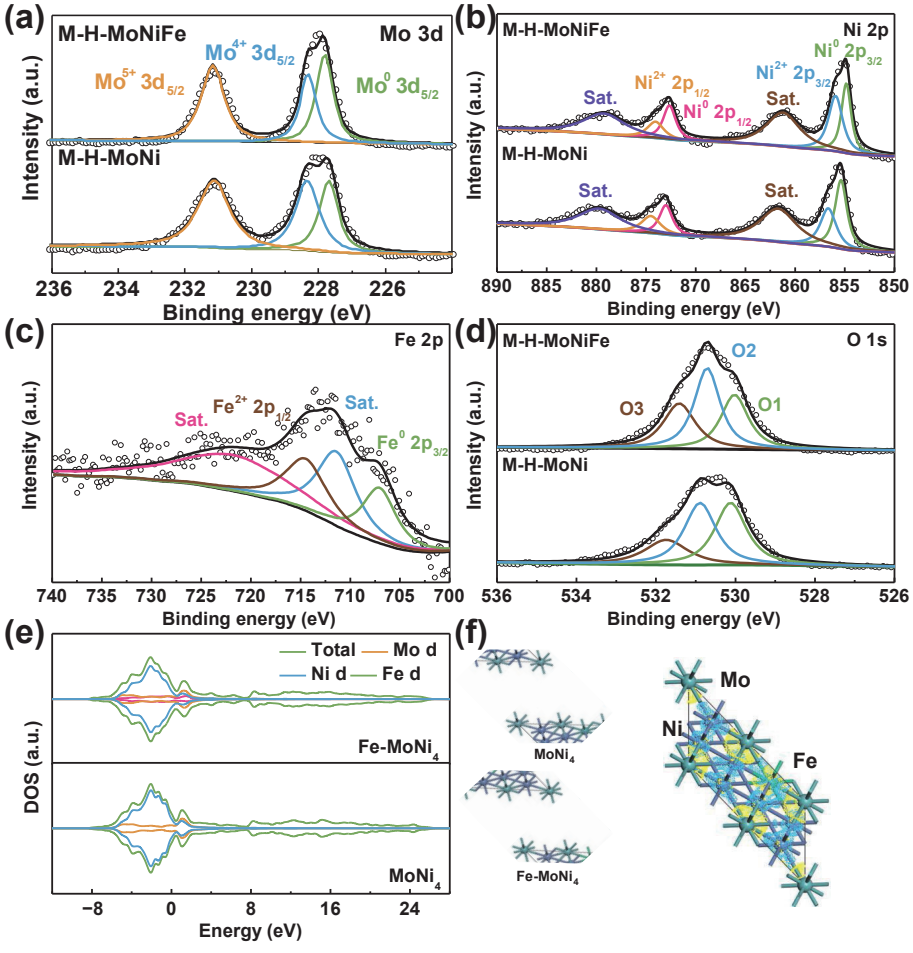

Figure 3 (a) Mo 3d, (b) Ni 2p, (c) Fe 2p, (d) O 1s of M-MoNiFe-50 and M-H-MoNiFe-50. (e) Calculated PDOS of $MoNi_4$, Fe-$MoNi_4$ and corresponding models. (f) Electron density difference simulation of Fe-$MoNi_4$. The cyan color indicates increased electron density while yellow color indicates decreased electron density.

microwave and Fe doping [16]. In terms of commercial application, durability is another vital criterion. Figure 4(e) depicts the chronopotentiometry results at the constant current density of 1,000 mA·cm^{-2}. During the whole hydrogen evolution process of 100 h, the measured *v*–*t* curves both show inconspicuous changes, which together with the morphologies and uniform Mo, Ni and Fe distribution after electrolysis verifies the outstanding durability due to the inherent structural robustness and strong adhesion between the material and substrate (Figs. S11 and S12 in the ESM).

Analogously, the HER performance of prepared samples was investigated in 0.5 M H_2SO_4 through a three-electrode system. The best-performing M-H-MoNiFe-50 was screened out as a target sample (Fig. S13 in the ESM). It should be pointed out that the Fe doped $MoNi_4$ alloy is considered to be the main active center for acidic HER. Encouragingly, the LSVs of M-H-MoNiFe-50 show the best HER activity, requiring only 23 and 254 mV at 10 and 1,000 mA·cm^{-2}, exceeding most previous catalysts (Fig. 4(f) and Table S3 in the ESM). The corresponding Tafel slopes show the smallest value of M-H-MoNiFe-50 (34.1 mV·dec^{-1}) near 30 mV·dec^{-1}, demonstrating that in acidic electrolyte the RDS is Tafel step, namely, the desorption of hydrogen control HER efficiency [33]. It can be seen from C_{dl} (Fig. S14(g) in the ESM) that the increased ECSA is the main reason for high HER activity in acidic media. EIS results further confirm higher conductivity than M-H-MoNi-50 and H-H-MoNiFe-300. The elevated electron transfer rate is contributed to the simultaneous regulation of microwave and intimate electron interaction between Fe and Mo, Ni. Moreover, chronopotentiometry was applied to study the durability of M-H-MoNiFe-50 in acidic media. The obtained *v*–*t* curve (Fig. 4(j)) shows that M-H-MoNiFe-50 can steadily produce hydrogen for 100 h at 100 and 200 mA·cm^{-2}, and only negligible HER performance degradation can be perceived. Besides, the morphology after the stability test suffers from inevitable dissolution due to the MoNi oxides. Nevertheless, the main nanorod assemblies are still maintained to the greatest extent (Fig. S11(b) in the ESM), again verifying the admirable stability of M-H-MoNiFe-50 sample. The TEM mapping, as shown in Fig. S12(b) in the ESM, also verifies the stability of M-H-MoNiFe-50 with the uniformly distributed Mo, Ni and Fe elements. Furthermore, the LSV curve after 5,000 CV cycles reveals good cyclic stability under wide pH range (Fig. S15 in the ESM).

Considering that dual-functional catalysts for HER and OER are more favorable for practical application, we then conducted the OER performance test in 1.0 M KOH. The microwave time was first adjusted to explore the influence of pretreatment on OER activity, and the same variation trend as that of HER was obtained (Fig. S16(a) in the ESM). M-H-MoNiFe-50 and H-H-MoNiFe-300 show similar OER performance and are both motivated after calcination, to reach the current density of 10 mA·cm^{-2} only needing an overpotential of 160 mV, lower than those of other electrocatalysts in previous work and commercial RuO_2 (Figs. 5(a) and 5(b), and Table S4 in the ESM).

It has been well-documented that OER materials under alkaline would suffer from inevitable oxidation accompanied by an amorphous structure.

In addition, for $NiMoO_4$, the leaching of Mo species is bound to happen under appropriate conditions [34, 35]. The role of $MoNi_4$ alloys and the real active sites in M-H-MoNiFe-50 for water oxidation is worth investigating. Tafel slopes were calculated and

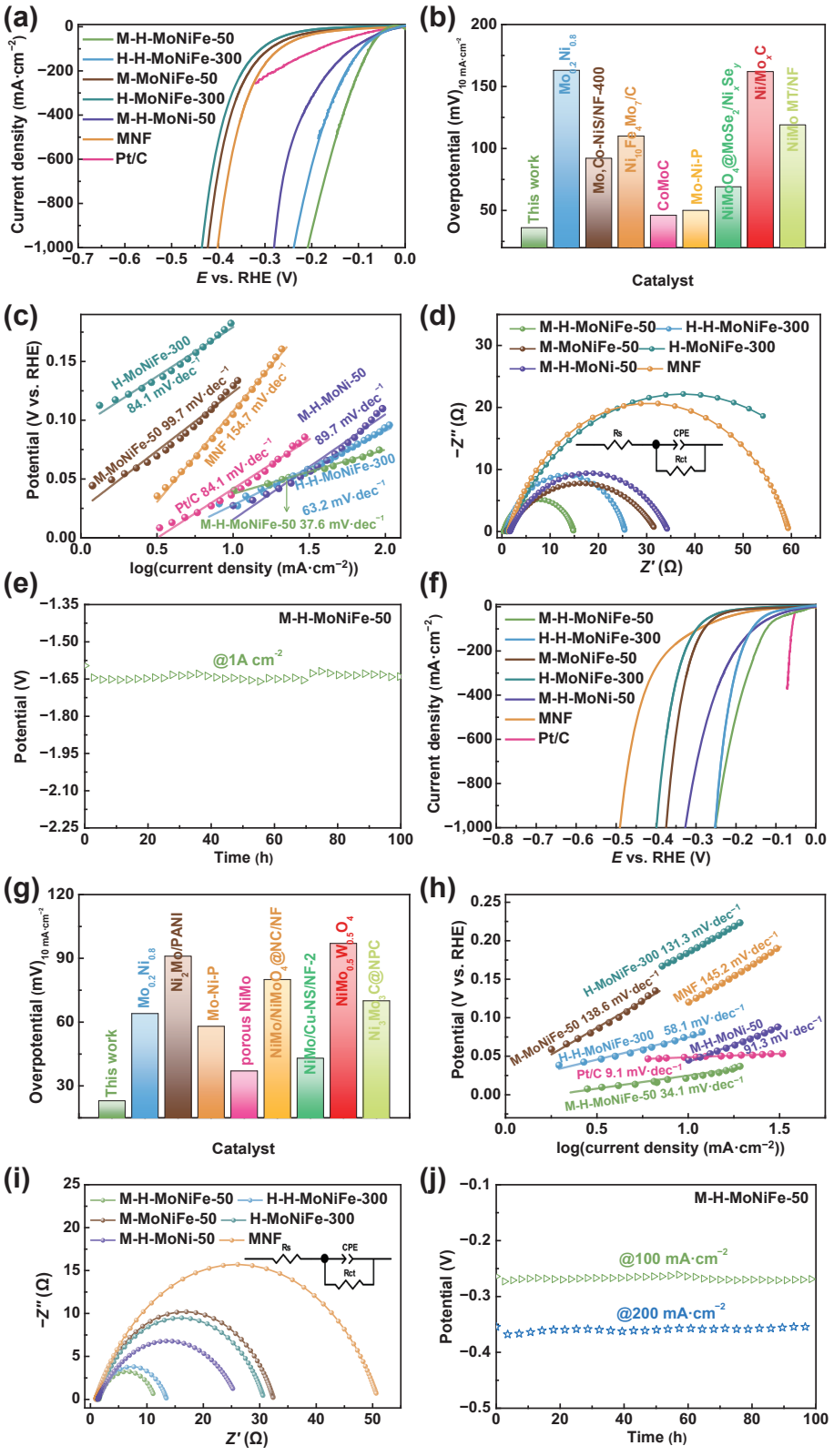

Figure 4 Electrochemical measurements of synthesized samples for HER in ((a)–(e)) 1.0 M KOH and ((f)–(j)) 0.5 M H_2SO_4. (a) LSVs, (c) Tafel plots, (d) EIS plots and (e) chronopotentiometry at 1 A·cm^{-2} in 1.0 M KOH; (f) LSVs, (h) Tafel plots, (i) EIS plots and (j) chronopotentiometry at 100 and 200 mA·cm^{-2} in 0.5 H_2SO_4. Comparisons of overpotential at 10 mA·cm^{-2} between M-H-MoNiFe-50 and reported catalysts in (b) 1.0 M KOH, and (g) 0.5 M H_2SO_4.

fitted to shed light on the reaction kinetics. As given in Fig. 5(c), M-H-MoNiFe-50 and H-H-MoNiFe-300 own similar slopes of 73.1 and 89.4 mV·dec^{-1}, respectively, suggesting their OER efficiencies are both restricted by the first electron/proton reaction (M + OH^- → M-OH + e^- and M-OH → M-OH*) and energy optimization of OH reactants, indicating the kinetically sluggish for the association of OH reactants on electrocatalytic active sites in the presence of obtained catalysts [36–38]. C_{dl} and EIS were studied to further clarify the role of Fe doping and microwave treatment. It is found that the increased ECSA is conducive to the high OER activity, since the rapid heating of microwave enables the well-maintained structure of M-H-MoNiFe-50 (Fig. S17(g) in the ESM). EIS (Fig. 5(d)) gives the information on OER kinetics. Interestingly, the final M-H-MoNiFe-50 possesses a much smaller impedance than

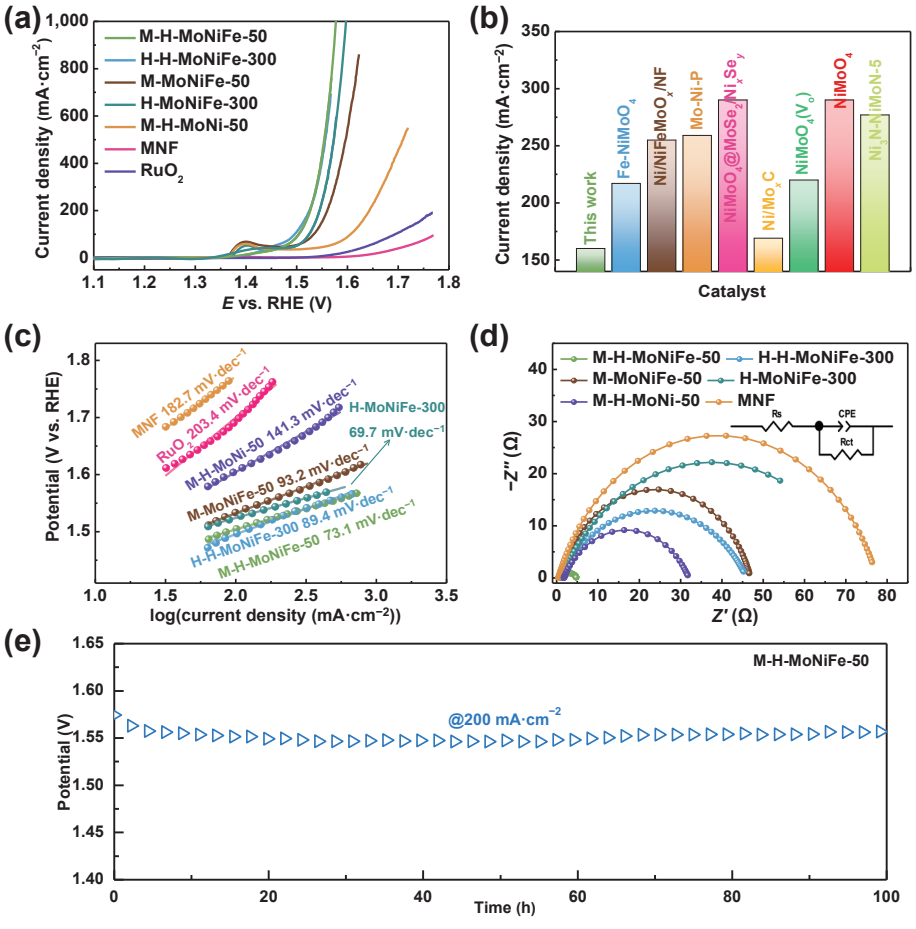

Figure 5 Electrochemical measurements of synthesized samples for OER in 1.0 M KOH. (a) LSVs, (c) Tafel plots, (d) EIS plots, and (e) chronopotentiometry at 200 mA·cm^{-2}. (b) Comparison of overpotential at 10 mA·cm^{-2} between M-H-MoNiFe-50 and reported catalysts.

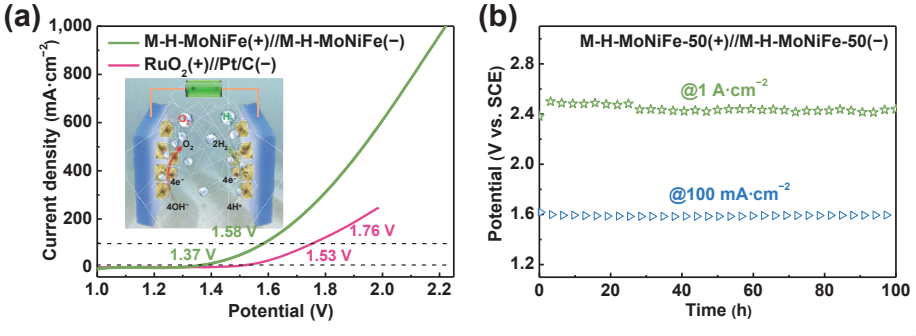

Figure 6 Electrocatalytic overall water splitting performance of assembled M-H-MoNiFe-50(+)//M-H-MoNiFe-50(−). (a) LSVs, insert: schematic diagram of two-electrode system. (b) Chronopotentiometric curves at 100 and 1,000 mA·cm^{-2}.

H-H-MoNiFe-50 and other control samples, which is consistent with HER results. Figure 5(e) shows that the M-H-MoNiFe-50 can run stably for 100 h at 200 mA·cm^{-2}, revealing great OER durability. In addition, the Mo, Ni and Fe elements are uniformly distributed on the selected region of M-H-MoNiFe-50 (Fig. S12(c) in the ESM).

In view of the excellent HER and OER activity, the OWS in 1.0 KOH was also measured using M-H-MoNiFe-50 as the anode and cathode. Inspiringly, the assembled M-H-MoNiFe-50(+)//M-H-MoNiFe-50(−) requires low overpotentials of 1.37 and 1.58 V at 10 and 100 mA·cm^{-2}, better than RuO_2(+)//Pt/C(−) electrode (Fig. 6(a)). More importantly, M-H-MoNiFe-50(+)//M-H-MoNiFe-50(−) can steadily operate for 100 h under constant 100 mA·cm^{-2} and high current density of 1,000 mA·cm^{-2}, respectively, without obvious performance degradation (Fig. 6(b)). The low potential, inherent robustness and high chemical stability mainly account for the excellent durability.

3.3 The role of Fe doping

In order to set forth the real active species, the XPS characterization of M-H-MoNiFe-50 after long-term stability was employed to uncover the changes of the electronic distribution and valence state. After electrolysis, Mo, Ni and Fe elements can also be observed (Fig. S18(a) in the ESM). For HER, the contents of Mo^{4+} notably increase, and the Mo 3d peaks move to higher binding energy, showing the oxidation of Mo, which is opposite to Ni 2p while similar to Fe 2p (Figs. 7(a)–7(c)).

When it comes to OER, the contents of Mo^{4+} sharply increase and the binding energies of Ni 2p and Mo 3d undergo a positive shift (Figs. 7(d) and 7(e)), suggesting that the higher oxidation states of Ni and Mo have been generated. Accordingly, a negative movement of Fe 2p is observed (Fig. 7(f)). Besides, no new valence state is deconvoluted. Those results indicate that for OER, high-valence Ni and Fe are the real active sites. To have a deep insight into the tailoring of Fe incorporation for electronic structure and

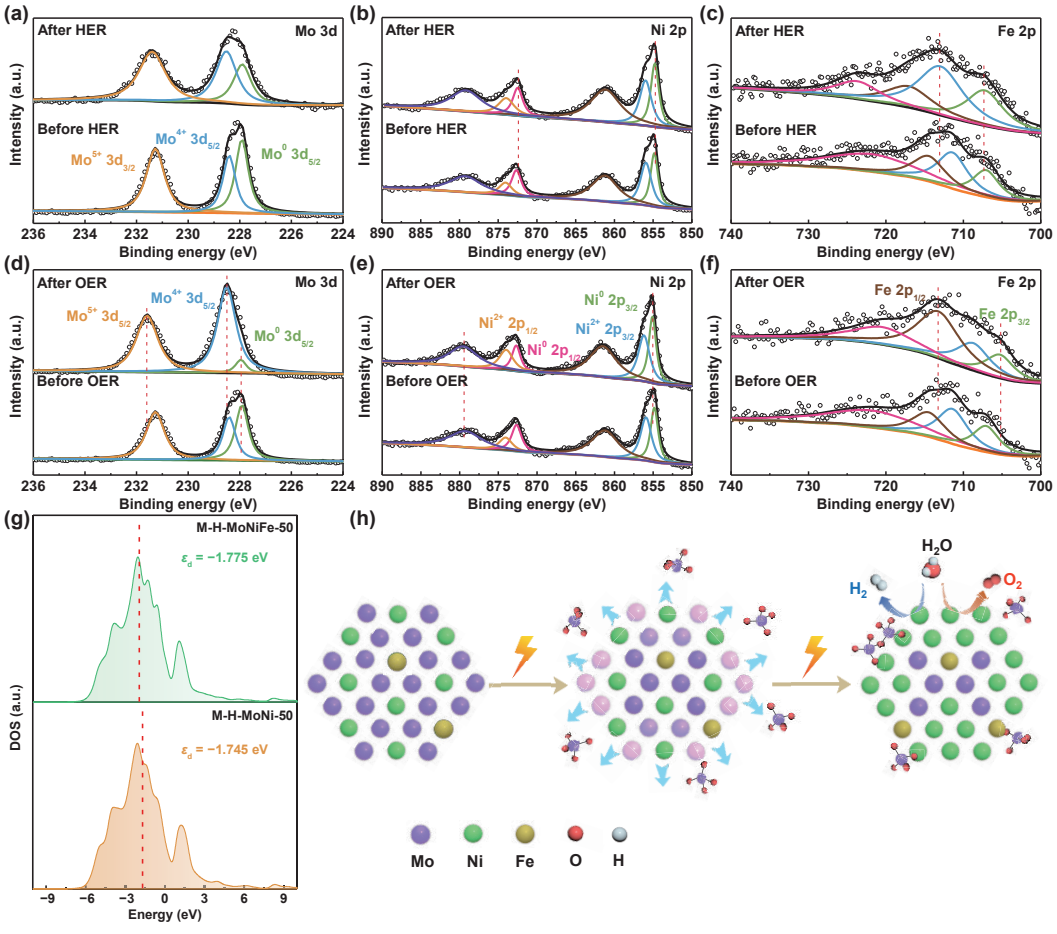

Figure 7 (a) Mo 3d, (b) Ni 2p, and (c) Fe 2p of M-H-MoNiFe-50 before and after long-term HER stability in alkaline media. (d) Mo 3d, (e) Ni 2p, and (f) Fe 2p of M-H-MoNiFe-50 before and after OER stability. (g) PDOS of the d orbitals of M-H-MoNiFe-50 with and without Fe. (h) Illustration of the behaviors of Mo in Fe doped $MoNi_4$ during alkaline OWS.

adsorbate–metal interaction, the energy level of the d-band center (ε_d) is also calculated (Fig. 7(g)). The d-state of M-H-MoNiFe-50 is far away from the Fermi level after Fe doping, thus increasing the ε_d accordingly. The ε_d energy level of M-H-MoNiFe-50 is computed to be −1.776 eV compared to that of M-H-MoNi-50 (−1.746 eV). The lower ε_d indicates the decreased antibonding energy states and weakened interaction between adsorbates and target M-H-MoNiFe-50 samples, which is propitious to the decline in adsorption ability for reaction intermediates to finally promote the hydrogen spillover and H_2 production [39, 40]. In addition, the Mo contents in M-H-MoNiFe-50 after HER and OER were analyzed (Table S1 in the ESM), falling of Mo content was detected in both of them. Recently, Zhang et al found that Mo in $MoNi_4$ would be oxidized and leached in the form of MoO_4^{2-} in the alkaline HER process because of more negative redox potential of Mo/MoO_4^{2-} [41]. The $MoNi_4$ alloy, adsorption of $Mo_2O_7^{2-}$ and roughened surface are deemed crucial for HER activity [41]. At present, three main mechanisms for HER of Mo-Ni alloys have been proposed, concretely, surface modification via Mo leaching [42], appropriate reaction energetics [43] on the Mo-Ni interface and Mo acting as an overflow "valve" to inhibit the deactivation of Ni hydride [44]. Based on these results, we postulate that in the process of HER electrolysis, $MoNi_4$ dissociates and produces MoO_4^{2-} species which can re-polymerize to $Mo_2O_7^{2-}$ in alkaline solution to ensure the stable progress of hydrogen evolution (Fig. 7(h)). It should be mentioned that the hydrogen capture and sink functions of Mo can protect the alloy system from deactivation by preventing the formation of subsurface hydrogen species. In stark contrast to HER, Mo suffers from more severe dissolution during oxygen evolution due to a high operating potential, enabling the generation of high valence Ni/Fe species more easily, thus forming Mo doped NiFeOOH compounds [34].

Furthermore, the possible spillover was researched and confirmed by temperature-programmed reduction (TPR) and temperature-programmed desorption (TPD) measurements. It is worth mentioning that the only notable difference between M-MoNiFe-50 precursor and final M-MoNiFe-50 sample lines in the newly generated MoNi alloys; therefore, it is acceptable to confirm the spillover phenomenon directly using the TPR and TPD of the two materials. Figure 8(a) shows the H_2-TPR results of M-MoNiFe-50 and M-MoNiFe-50 samples. The TPR signals around 430, 540, and 740 °C can be assigned to the H_2 desorption from NiO_2, $NiMoO_4$, MoO_2 and other species that are difficult to reduce [45, 46]. The slightly negative shifted temperature of M-MoNiFe-50 generally implies the presence of hydrogen spillover [47]. Besides, the new peak at low temperature (~ 282 °C) is the H_2 desorption from MoO_2 on the surface, which shows direct evidence of the spillover of hydrogen from Ni to Mo. The O_2-TPR curves in Fig. 8(b) show a distinctive difference. A strong oxygen desorption peak appears at ~ 590 °C accompanied by a shoulder peak, which is related to the $MoNi_4$ alloys. In addition, compared with M-MoNiFe-50, M-H-MoNiFe-50 possesses a unique wide desorption peak at 100–200 °C of weakly adsorbed oxygen species, suggesting that oxygen spills from $MoNi_4$ to the surface of catalyst [47–49]. These characterizations prove that the spillover of hydrogen and oxygen does exist in obtained M-H-MoNiFe-50 sample.

The H–D exchange between D_2 and hydroxyl groups on the substrates of catalysts has also been employed to detect spilled hydrogen. The hydrogen diffusion can be related to the rate of

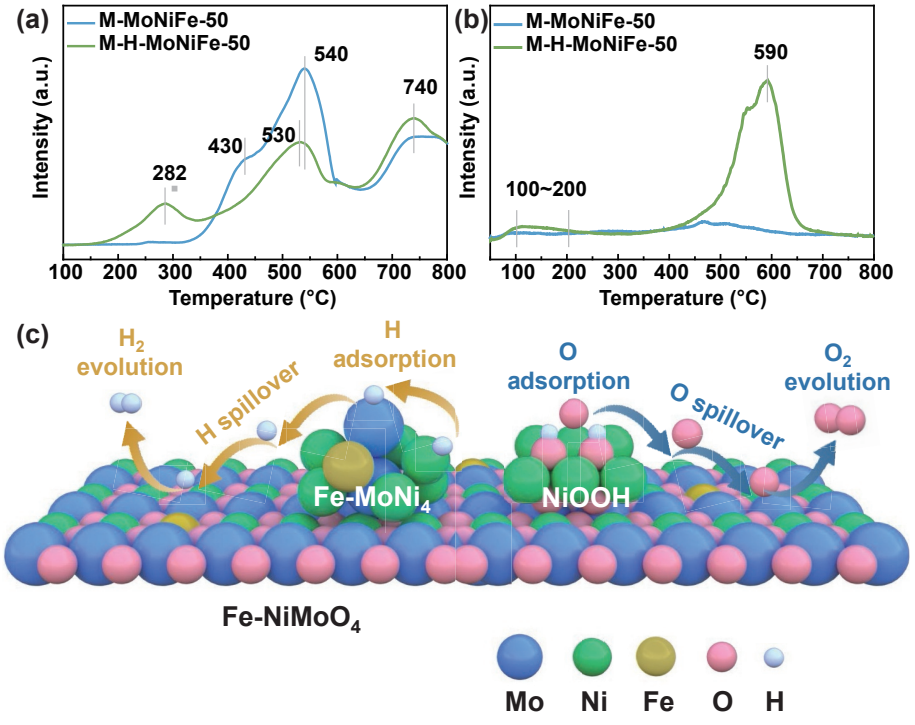

Figure 8 (a) H_2-TPR and (b) O_2-TPD of M-MoNiFe-50 and M-H-MoNiFe-50 samples. (c) Schematic illustration of hydrogen/oxygen spillover from Ni to Mo species in M-H-MoNiFe-50 catalyst.

H_2/D_2 equilibration and spillover. The activation energy of surface diffusion ranging about 10–25 kJ·mol^{-1} only accounts for a few portions of molecular desorption, and thus the diffusion coefficient at room temperature is around 10^{-5} cm^{-2}·s^{-1}, meaning that the hydrogen movement is almost instantaneous. Therefore, the mechanism of spillover can be postulated as follows: For hydrogen spillover, the synergy of M-H-MoNiFe-50 is well-modulated via fast intra- and inter-particle surface diffusion of H atoms, where the Ni/Fe acts as the hydrogen source for a neighboring Mo "trap center" and affects the initial proton discharge, by which the hydrogen desorption can be boosted effectively [44]. For oxygen spillover, the electron transfer is regarded to be the primary driving force, which plays a role in compensating for the charge accumulation caused by nucleophilic oxygen transfer [15]. The NiOOH can be the oxidation center and tends to release oxygen. Meanwhile, the MoO_x becomes the destination of the overflow oxygen. Hence, we deduce that the Fe-$MoNi_4$ alloys obtain electrons from Mo species, which in turn drive the nucleophilic oxygen that is adsorbed on NiOOH to transfer to (Ni)MoO_x (mainly MoO_x and some unreconstructed NiO_x). Through the efficient desorption of intermediates, the electrocatalytic performance can be elevated to a certain extent. These results all convince that microwave pretreatment and subsequent reduction reactions endow M-H-MoNiFe-50 with favorable HER, OER and OWS performances under large current density, which are benefited from the synergistic effect of tailored electron distribution, inherently stable structure and modified surface by Mo dissolution as well as an accompanying spillover effect.

4 Conclusions

In summary, abundant flower-like M-H-MoNiFe-50 nanorod assemblies were fabricated on MoNi foam successively via an unconventional high-pressure microwave hydrothermal method followed by calcination in H_2/Ar. The vertical nanorods anchored with numerous Fe-doped $MoNi_4$ nanoparticles enable the transfer and access of electrolyte ions much easier. In addition, the higher areal density of nanopillars and redistributed electronic structure are also conferred thanks to the microwave fast heating and Fe doping. Besides, the unique structure has been proven to be favorable for the spillover effect to boost catalytic performance. The obtained M-H-MoNiFe-50 exhibits superior HER, OER and OWS activities under large current density. In detail, for HER, 208 mV (in alkaline) and 254 mV (in acidic) are required at 1,000 mV·cm^{-2}, respectively. For OER, only 160 mV can reach the density of 10 mA·cm^{-2}. With respect to OWS, using M-H-MoNiFe-50 as the anode and cathode, 10 and 100 mA·cm^{-2} are achieved at 1.37 and 1.58 V. More importantly, under alkaline electrolyte, M-H-MoNiFe-50(+)//M-H-MoNiFe-50(−) can produce hydrogen steadily for 50 h at 1,000 mA·cm^{-2}. The resulting electrocatalysts of water splitting show great potential for commercial application and demonstrate the significant enhancement of Fe doping, microwave and spillover for catalytic performance.

Acknowledgements

This work was financially supported by the National Natural Science Foundation of China (No. 52174283) and Qingdao Science and Technology Benefiting People Special Project (No. 20-3-4-8-nsh), the Fundamental Research Funds for the Central Universities (No. 20CX02212A), the Development Fund of State Key Laboratory of Heavy Oil Processing and the Postgraduate Innovation Project of China University of Petroleum (No. YCX2020046).

Electronic Supplementary Material: Supplementary material (SEM, electrochemical measurements, element contents, and supplementary tables) is available in the online version of this article at https://doi.org/10.1007/s12274-022-4230-9.

References

[1] Rong, H. P.; Ji, S. F.; Zhang, J. T.; Wang, D. S.; Li, Y. D. Synthetic strategies of supported atomic clusters for heterogeneous catalysis. *Nat. Commun.* **2020**, *11*, 5884.

[2] Zhang, N. Q.; Ye, C. L.; Yan, H.; Li, L. C.; He, H.; Wang, D. S.; Li,

Y. D. Single-atom site catalysts for environmental catalysis. *Nano Res.* **2020**, *13*, 3165–3182.
[3] Gao, X. Q.; Chen, Y. D.; Sun, T.; Huang, J. M.; Zhang, W.; Wang, Q.; Cao, R. Karst landform-featured monolithic electrode for water electrolysis in neutral media. *Energy Environ. Sci.* **2020**, *13*, 174–182.
[4] Zhou, Y. N.; Wang, F. L.; Dou, S. Y.; Shi, Z. N.; Dong, B.; Yu, W. L.; Zhao, H. Y.; Wang, F. G.; Yu, J. F.; Chai, Y. M. Motivating high-valence Nb doping by fast molten salt method for NiFe hydroxides toward efficient oxygen evolution reaction. *Chem. Eng. J.* **2022**, *427*, 131643.
[5] Yin, J.; Jin, J.; Lu, M.; Huang, B. L.; Zhang, H.; Peng, Y.; Xi, P. X.; Yan, C. H. Iridium single atoms coupling with oxygen vacancies boosts oxygen evolution reaction in acid media. *J. Am. Chem. Soc.* **2020**, *142*, 18378–18386.
[6] Zhang, J. Y.; Yan, Y.; Mei, B. B.; Qi, R. J.; He, T.; Wang, Z. T.; Fang, W. S.; Zaman, S.; Su, Y. Q.; Ding, S. J. et al. Local spin-state tuning of cobalt-iron selenide nanoframes for the boosted oxygen evolution. *Energy Environ. Sci.* **2021**, *14*, 365–373.
[7] Zou, X.; Liu, Y. P.; Li, G. D.; Wu, Y. Y.; Liu, D. P.; Li, W.; Li, H. W.; Wang, D. J.; Zhang, Y.; Zou, X. X. Ultrafast formation of amorphous bimetallic hydroxide films on 3D conductive sulfide nanoarrays for large-current-density oxygen evolution electrocatalysis. *Adv. Mater.* **2017**, *29*, 1700404.
[8] Lagadec, M. F.; Grimaud, A. Water electrolysers with closed and open electrochemical systems. *Nat. Mater.* **2020**, *19*, 1140–1150.
[9] Yang, J. R.; Li, W. H.; Wang, D. S.; Li, Y. D. Electronic metal-support interaction of single-atom catalysts and applications in electrocatalysis. *Adv. Mater.* **2020**, *32*, 2003300.
[10] Gao, X. Q.; Chen, D. D.; Qi, J.; Li, F.; Song, Y. J.; Zhang, W.; Cao, R. NiFe oxalate nanomesh array with homogenous doping of Fe for electrocatalytic water oxidation. *Small* **2019**, *15*, 1904579.
[11] Zhang, W.; Wu, Y. Z.; Qi, J.; Chen, M. X.; Cao, R. A thin NiFe hydroxide film formed by stepwise electrodeposition strategy with significantly improved catalytic water oxidation efficiency. *Adv. Energy Mater.* **2017**, *7*, 1602547.
[12] Highfield, J. G.; Claude, E.; Oguro, K. Electrocatalytic synergism in Ni/Mo cathodes for hydrogen evolution in acid medium: A new model. *Electrochim. Acta* **1999**, *44*, 2805–2814.
[13] Kamp, C. J.; Garza, H. H. P.; Fredriksson, H.; Kasemo, B.; Andersson, B.; Skoglundh, M. Nanofabricated catalyst particles for the investigation of catalytic carbon oxidation by oxygen spillover. *Langmuir* **2017**, *33*, 4903–4912.
[14] Ananyev, M. V.; Porotnikova, N. M.; Eremin, V. A.; Kurumchin, E. K. Interaction of O_2 with LSM-YSZ composite materials and oxygen spillover effect. *ACS Catal.* **2021**, *11*, 4247–4262.
[15] Zhao, D. H.; Pan, Y. M.; Zang, Y. R.; Zhao, X. Z. A kinetic and quantum chemical investigation of oxygen spillover from α-Sb_2O_4 to MoO_3. *Chin. J. Catal.* **1996**, *17*, 133–138.
[16] Slocombe, D. R. Cool water splitting by microwaves. *Nat. Energy* **2020**, *5*, 830–831.
[17] Zhang, H. M.; Lee, J. S. Hybrid microwave annealing synthesizes highly crystalline nanostructures for (photo)electrocatalytic water splitting. *Acc. Chem. Res.* **2019**, *52*, 3132–3142.
[18] Serra, J. M.; Borrás-Morell, J. F.; García-Baños, B.; Balaguer, M.; Plaza-González, P.; Santos-Blasco, J.; Catalán-Martínez, D.; Navarrete, L.; Catalá-Civera, J. M. Hydrogen production via microwave-induced water splitting at low temperature. *Nat. Energy* **2020**, *5*, 910–919.
[19] Zhang, J.; Wang, T.; Liu, P.; Liao, Z. Q.; Liu, S. H.; Zhuang, X. D.; Chen, M. W.; Zschech, E.; Feng, X. L. Efficient hydrogen production on $MoNi_4$ electrocatalysts with fast water dissociation kinetics. *Nat. Commun.* **2017**, *8*, 15437.
[20] Qin, J. F.; Yang, M.; Chen, T. S.; Dong, B.; Hou, S.; Ma, X.; Zhou, Y. N.; Yang, X. L.; Nan, J.; Chai, Y. M. Ternary metal sulfides MoCoNiS derived from metal organic frameworks for efficient oxygen evolution. *Int. J. Hydrogen Energy* **2020**, *45*, 2745–2753.
[21] Yan, X. X.; Gu, M. Y.; Wang, Y.; Xu, L.; Tang, Y. W.; Wu, R. B. *In-situ* growth of Ni nanoparticle-encapsulated N-doped carbon nanotubes on carbon nanorods for efficient hydrogen evolution electrocatalysis. *Nano Res.* **2020**, *13*, 975–982.
[22] Zhang, W.; Qi, J.; Liu, K. Q.; Cao, R. A nickel-based integrated electrode from an autologous growth strategy for highly efficient water oxidation. *Adv. Energy Mater.* **2016**, *6*, 1502489.
[23] Gong, L. Q.; Yang, H.; Wang, H. M.; Qi, R. J.; Wang, J. L.; Chen, S. H.; You, B.; Dong, Z. H.; Liu, H. F.; Xia, B. Y. Corrosion formation and phase transformation of nickel-iron hydroxide nanosheets array for efficient water oxidation. *Nano Res.* **2021**, *14*, 4528–4533.
[24] Hu, W. B.; Liu, Y.; Withers, R. L.; Frankcombe, T. J.; Norén, L.; Snashall, A.; Kitchin, M.; Smith, P.; Gong, B.; Chen, H. et al. Electron-pinned defect-dipoles for high-performance colossal permittivity materials. *Nat. Mater.* **2013**, *12*, 821–826.
[25] Wang, Z.; Wang, W. Z.; Zhang, L.; Jiang, D. Surface oxygen vacancies on Co_3O_4 mediated catalytic formaldehyde oxidation at room temperature. *Catal. Sci. Technol.* **2016**, *6*, 3845–3853.
[26] Mao, C. L.; Wang, J. X.; Zou, Y. J.; Qi, G. D.; Loh, J. Y. Y.; Zhang, T. H.; Xia, M. K.; Xu, J.; Deng, F.; Ghoussoub, M. et al. Hydrogen spillover to oxygen vacancy of $TiO_{2-x}H_y$/Fe: Breaking the scaling relationship of ammonia synthesis. *J. Am. Chem. Soc.* **2020**, *142*, 17403–17412.
[27] Fang, Y. H.; Liu, Z. P. Tafel kinetics of electrocatalytic reactions: From experiment to first-principles. *ACS Catal.* **2014**, *4*, 4364–4376.
[28] Anantharaj, S.; Noda, S.; Driess, M.; Menezes, P. W. The pitfalls of using potentiodynamic polarization curves for Tafel analysis in electrocatalytic water splitting. *ACS Energy Lett.* **2021**, *6*, 1607–1611.
[29] De Chialvo, M. R. G.; Chialvo, A. C. Kinetics of hydrogen evolution reaction with Frumkin adsorption: Re-examination of the Volmer-Heyrovsky and Volmer-Tafel routes. *Electrochim. Acta* **1998**, *44*, 841–851.
[30] Shinagawa, T.; Garcia-Esparza, A. T.; Takanabe, K. Insight on Tafel slopes from a microkinetic analysis of aqueous electrocatalysis for energy conversion. *Sci. Rep.* **2015**, *5*, 13801.
[31] Guan, C.; Xiao, W.; Wu, H. J.; Liu, X. M.; Zang, W. J.; Zhang, H.; Ding, J.; Feng, Y. P.; Pennycook, S. J.; Wang, J. Hollow Mo-doped CoP nanoarrays for efficient overall water splitting. *Nano Energy* **2018**, *48*, 73–80.
[32] Chi, J. Q.; Zhang, X. Y.; Ma, X.; Dong, B.; Zhang, J. Q.; Guo, B. Y.; Yang, M.; Wang, L.; Chai, Y. M.; Liu, C. G. Interface charge engineering of ultrafine Ru/Ni_2P nanoparticles encapsulated in N, P-codoped hollow carbon nanospheres for efficient hydrogen evolution. *ACS Sustainable Chem. Eng.* **2019**, *7*, 17714–17722.
[33] Tian, X. Y.; Zhao, P. C.; Sheng, W. C. Hydrogen evolution and oxidation: Mechanistic studies and material advances. *Adv. Mater.* **2019**, *31*, 1808066.
[34] Yu, L.; Zhou, T. T.; Cao, S. H.; Tai, X. S.; Liu, L. L.; Wang, Y. Suppressing the surface passivation of Pt-Mo nanowires via constructing Mo-Se coordination for boosting HER performance. *Nano Res.* **2021**, *14*, 2659–2665.
[35] Duan, Y.; Yu, Z. Y.; Hu, S. J.; Zheng, X. S.; Zhang, C. T.; Ding, H. H.; Hu, B. C.; Fu, Q. Q.; Yu, Z. L.; Zheng, X. et al. Scaled-up synthesis of amorphous NiFeMo oxides and their rapid surface reconstruction for superior oxygen evolution catalysis. *Angew. Chem., Int. Ed.* **2019**, *58*, 15772–15777.
[36] Cui, B. H.; Hu, Z.; Liu, C.; Liu, S. L.; Chen, F. S.; Hu, S.; Zhang, J. F.; Zhou, W.; Deng, Y. D.; Qin, Z. B. et al. Heterogeneous lamellar-edged Fe-Ni$(OH)_2$/Ni_3S_2 nanoarray for efficient and stable seawater oxidation. *Nano Res.* **2021**, *14*, 1149–1155.
[37] Yan, M. L.; Zhao, Z. Y.; Cui, P. X.; Mao, K.; Chen, C.; Wang, X. Z.; Wu, Q.; Yang, H.; Yang, L. J.; Hu, Z. Construction of hierarchical $FeNi_3$@(Fe, Ni)S_2 core-shell heterojunctions for advanced oxygen evolution. *Nano Res.* **2021**, *14*, 4220–4226.
[38] Wang, T. J.; Liu, X. Y.; Li, Y.; Li, F. M.; Deng, Z. W.; Chen, Y. Ultrasonication-assisted and gram-scale synthesis of Co-LDH nanosheet aggregates for oxygen evolution reaction. *Nano Res.* **2020**, *13*, 79–85.
[39] Wei, Z. W.; Wang, H. J.; Zhang, C.; Xu, K.; Lu, X. L.; Lu, T. B. Reversed charge transfer and enhanced hydrogen spillover in

platinum nanoclusters anchored on titanium oxide with rich oxygen vacancies boost hydrogen evolution reaction. *Angew. Chem., Int. Ed.* **2021**, *60*, 16622–16627.

[40] Sun, S. F.; Zhou, X.; Cong, B. W.; Hong, W. Z.; Chen, G. Tailoring the d-band centers endows $(Ni_xFe_{1-x})_2P$ nanosheets with efficient oxygen evolution catalysis. *ACS Catal.* **2020**, *10*, 9086–9097.

[41] Du, W.; Shi, Y. M.; Zhou, W.; Yu, Y. F.; Zhang, B. Unveiling the *in situ* dissolution and polymerization of Mo in Ni_4Mo alloy for promoting the hydrogen evolution reaction. *Angew. Chem., Int. Ed.* **2021**, *60*, 7051–7055.

[42] Liu, Z. Z.; Shang, X.; Dong, B.; Chai, Y. M. Triple Ni-Co-Mo metal sulfides with one-dimensional and hierarchical nanostructures towards highly efficient hydrogen evolution reaction. *J. Catal.* **2018**, *361*, 204–213.

[43] Schalenbach, M.; Speck, F. D.; Ledendecker, M.; Kasian, O.; Goehl, D.; Mingers, A. M.; Breitbach, B.; Springer, H.; Cherevko, S.; Mayrhofer, K. J. J. Nickel-molybdenum alloy catalysts for the hydrogen evolution reaction: Activity and stability revised. *Electrochim. Acta* **2018**, *259*, 1154–1161.

[44] Brito, J. L.; Laine, J. Reducibility of Ni-Mo/Al_2O_3 catalysts: A TPR study. *J. Catal.* **1993**, *139*, 540–550.

[45] Shang, H. Y.; Xu, Y. Q.; Zhao, H. J.; Liu, C. G. Study of carbon nanotube supported Co-Mo HDS catalysts. *J. Mol. Catal.* **2004**, *18*, 41–46.

[46] Nabaho, D.; Niemantsverdriet, J. W.; Claeys, M.; Van Steen, E. Hydrogen spillover in the Fischer-Tropsch synthesis: An analysis of platinum as a promoter for cobalt-alumina catalysts. *Catal. Today* **2016**, *261*, 17–27.

[47] Yao, Y. X.; Goodman, D. W. Direct evidence of hydrogen spillover from Ni to Cu on Ni-Cu bimetallic catalysts. *J. Mol. Catal. A: Chem.* **2014**, *383–384*, 239–242.

[48] Li, W. M.; Liu, H. D.; Zhang, M.; Chen, Y. F. Comparative study of mesoporous $Ni_xMn_{6-x}Ce_4$ composite oxides for NO catalytic oxidation. *RSC Adv.* **2019**, *9*, 31035–31042.

[49] Geng, S.; Liu, Y. Q.; Yu, Y. S.; Yang, W. W.; Li, H. B. Engineering defects and adjusting electronic structure on S doped MoO_2 nanosheets toward highly active hydrogen evolution reaction. *Nano Res.* **2020**, *13*, 121–126.